JOURNAL OF MATERIALS SCIENCE 28 (1993) 2438–2448

Fracture behaviour of glass-fibre mat-reinforced structural nylon RIM composites studied by microscopic and acoustic emission techniques

J. KARGER-KOCSIS and T. CZIGÁNY*
Institut für Verbundwerkstoffe GmbH, Universität Kaiserslautern, Pf. 3049,
D-6750 Kaiserslautern, Germany

The fracture and failure behaviour of continuous glass-fibre mat-reinforced nylon block copolymer were studied at monotonic increased loading at different temperatures ($T = -40$ to $80\,^{\circ}$C and deformation rates ($v = 1$ and $1000\,\mathrm{mm\,min^{-1}}$). The fracture toughness, K_c, was determined on compact tension specimens of different size in order to elucidate size effects. K_c increased with increasing glass-fibre mat content and with deformation rate, whereas increasing temperature resulted in lower K_c values. K_c was unaffected by the free ligament width of the compact tension specimens used. The failure manner was studied by acoustic emission and microscopic techniques (transmitted light and scanning electron microscopy). Simultaneous monitoring of the failure mode by acoustic emission and transmitted light microscopy allowed the failure sequence to be deduced and led to a reliable discrimination between the observed failure events based on their acoustic emission signal characteristics (e.g. amplitude, energy). For this composite with a very ductile thermoplastic matrix the following failure steps were concluded: (a) fibre debonding due to crack-tip blunting, (b) network-type deformation of the glass-fibre mat with concomitant fibre debonding and voiding of the matrix, (c) formation of kinked strands with crack opening due to matrix yielding, (d) fracture of the bent filaments within the strands followed by pull-out processes (fibre–fibre, fibre–matrix). The development of the damage zone was also assessed by acoustic emission via localization of the related events. It was established that the damage zone reaches its maximum dimension at the maximum load and only its shape changes along the crack-growth direction upon further loading.

---

1. Introduction

Although reaction injection moulding (RIM) of polyamide-6 (nylon) was developed a decade ago, this technique has only recently had an impact due to an increasing demand for thermoplastic matrix composites. Polyamide (PA) structural RIM (SRIM) products with continuous-fibre reinforcement (mostly in form of mats and fabrics) are of great interest for different engineering applications. The PA–SRIM technology unifies the production and forming procedures in one step, contrary to other thermoplastic-based composites with continuous-fibre reinforcement where these steps are always separated, i.e. production of preforms (prepregs, sheets, hybrid yarns or fabrics, etc.) and their processing into final parts (e.g. by thermoforming, pultrusion) are not connected. The wetting of the reinforcement, placed into the mould before filling, is excellent due to the very low melt viscosity of the PA–RIM system to be polimerized *in situ*. Because the polymerization is very fast, short demoulding cycles can be reached. The PA–RIM process is also very versatile from the matrix side, because nylon block copolymers (NBC) of different compositions with improved resistance to impact at low temperatures, are also available. The target application fields of PA–SRIM composites necessitate a profound characterization of the fracture, fatigue, stress corrosion cracking and related failure behaviour about which limited information is as yet available [1–6]. The aims of the investigations reported here were to determine whether the free ligament width of the compact tension (CT) specimens usually applied, affect the fracture mechanics values, to clarify the basic failure events and to distinguish between them and,

---

**Permanent address*: Institute of Machine Parts of the Technical University of Budapest, Hungary.

finally, to conclude the failure sequence and assess the damage zone in (swirl) glass-strand mat-reinforced NBC–SRIM composites.

2. Experimental procedure

2.1. Specimens

The plates investigated ($150 \times 150 \times 4$ mm^3) were produced by RAPRA Technology Ltd (Shawbury, UK) using components of the Nyrim^R 2000 system of DSM (Maastricht, The Netherlands). The matrix block copolymer (NBC) contained 20 wt% elastomeric polyether segments. E-glass-strand mat (Unifilo U816 swirl mat, Vetrotex International, Aix-les-Bains, France) was stacked into the mould prior to filling and thus the glass-fibre (GF) content was set in the range 20–50 wt%. This GF mat, of 450 g m^{-2} surface density, was sized by a silane compound and bonded by a polyester binder.

For the static fracture measurements, razor-blade notched compact tension (CT) specimens in two different dimensions were used. They differed from one another mainly in the free ligament width (W–a). The CT specimens were notched in both transverse (T) and longitudinal (L) directions with respect to that of mould filling (MFD) in order to investigate eventual anisotropic effects. The sum of the sawn and razor-blade introduced notch was treated as the initial notch (a; cf. Fig. 1) in the calculations. The cutting and dimensions of the CT specimens used are depicted schematically in Fig. 1.

2.2 Tests

Static fracture of the CT specimens was performed on a Zwick 1445-type tensile loading machine equipped with a thermostatic chamber. Loading occurred at two crosshead speeds, $v = 1$ and $= 1000$ mm min^{-1}, at different temperatures, $T = -40$, 20 and 80 °C. The critical stress intensity factor or fracture toughness, K_c, was determined according to the ASTM E 399 standard.

Fracture of the CT specimens was studied by transmitted light microscopy (TLM) during low-speed loading. This was possible due to the transparency of the NBC matrix, especially at lower GF mat contents. In order to distinguish between the failure events evidenced by light microscopy, the acoustic emission (AE) of the specimen was also monitored during loading.

AE was detected by a Defektophone NEZ 220 analyser (Central Research Institute for Physics, Budapest, Hungary) using wide bandwidth transducers (20–1000 kHz) with built-in preamplifier. The signals emanating from the sensor were amplified additionally by a logarithmic amplifier unit. AE events were collected throughout the loading tests either with one sensor or with a four-sensor array (cf. Fig. 1). The latter mode permitted the localization of the events based on the first-hit principle with knowledge of the acoustic-wave propagation speed determined previously. The positioning of the AE sensors on the CT specimens is also shown in Fig. 1. During the tests, the following primary AE signals were collected in floating mode and transferred for on-line data processing and storing to an IBM-PC by an RS-232 standard interface: elapsed time, ringdown count, rise time, event duration, peak amplitude, events number, absolute average and, in addition, the external parameter (force) from the tensile machine. The PC software enabled different processing and displaying of the data.

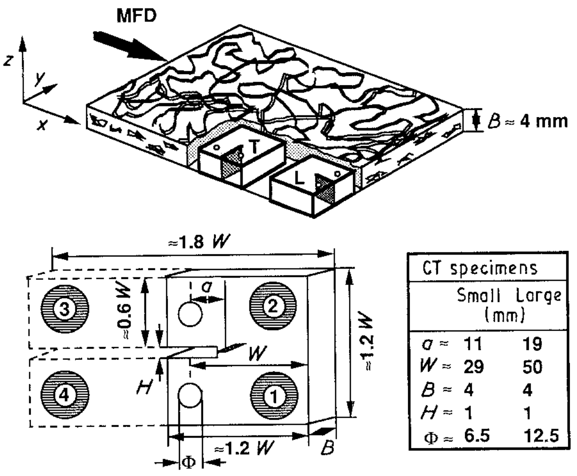

CT specimens	Small	Large
	(mm)	
$a \approx$	11	19
$W \approx$	29	50
$B \approx$	4	4
$H \approx$	1	1
$\Phi \approx$	6.5	12.5

Figure 1 Structure of the GF mat-reinforced SRIM composites shown schematically, as well as machining, dimensions and notching of the CT specimens used. The position of the AE sensors in localization-mode can also be seen on the modified large CT specimen. Localization of the AE events was performed only on modified, large CT specimens. In the tests with one AE sensor, the transducer was attached in position 1.

Failure was also investigated by *post mortem* fractographic analysis in a Leitz 1600 T scanning electron microscope (SEM). To avoid charging, the samples were coated either with gold or carbon. The latter samples were used for energy dispersive analysis by X-rays (EDAX).

3. Results and discussion

3.1. Fracture toughness

Fig 2 indicates that increasing GF mat content improves the fracture toughness considerably. Incorporation of about 50 wt% GF mat yields a 4–6 times increase in K_c depending on the crosshead speed and temperature. Increasing the crosshead speed resulted in higher fracture toughness values for both matrix and composites. Such a matrix behaviour is rather characteristic for impact-modified unfilled thermoplastics [7] to which group the NBC studied belongs. On the other hand, the observed trend for the composites is rather peculiar, because increasing deformation rate is generally accompanied by a drop in K_c, at least for chopped-fibre reinforced PA composites [7]. It should be noted here, that the thickness of the NBC matrix did not allow the determination of real plane strain fracture toughness values, therefore their designation should be correctly K_Q. K_Q values of the NBC were calculated by considering the 5% offset value of the initial compliance in the force–load line displacement (F–v_{LL}) curve. In contrary to the matrix,

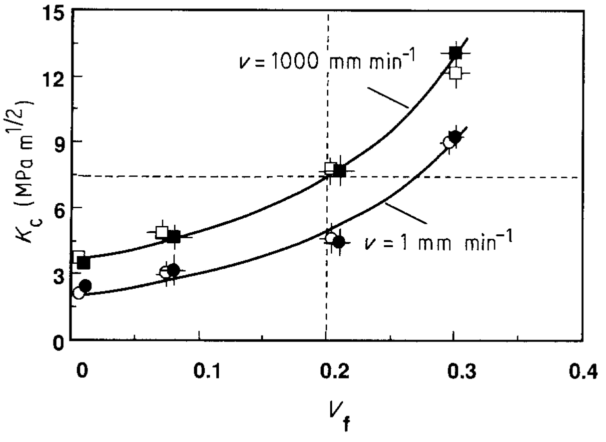

Figure 2 K_c as a function of the GF mat volume fraction, V_f, at monotonic increased static loading for (○, □) small and (●, ■) large CT specimens at room temperature (RT) as a function of the crosshead speed. The scatter range indicates the effects of the notching direction (L and T, cf. Fig. 1)

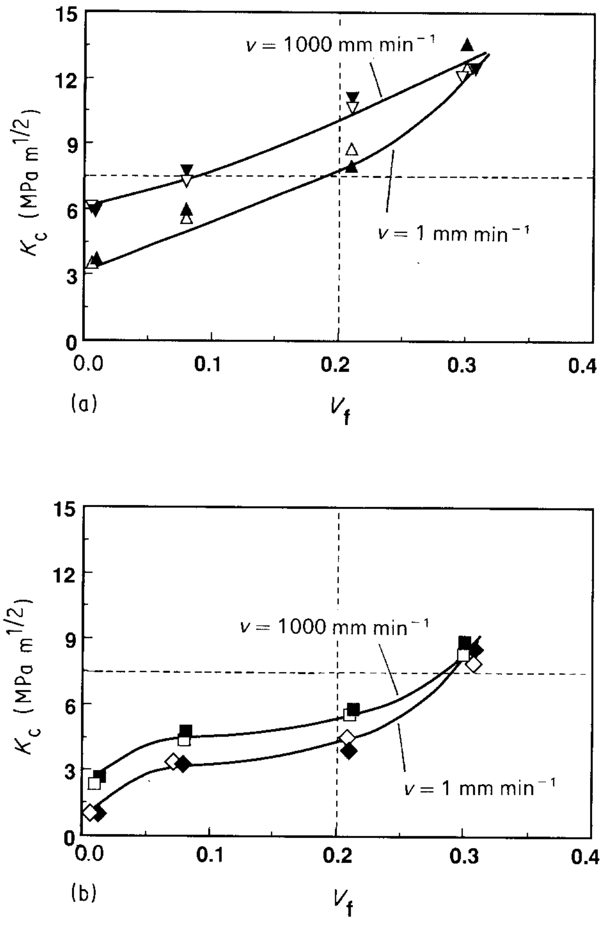

Figure 3 K_c as a function of the GF mat volume fraction, V_f at monotonic increased static loading for small (△, ▽, ◇, □) and large (▲, ▼, ◆, ■) CT specimens at crosshead speeds of (△, ▲, ◇, ◆) 1 and (▽, ▼, □, ■) 1000 mm min^{-1}, at (a) $T = -40$ °C, (b) $T = 80$°C.

the composites met the size criteria of the ASTM E 399 standard under all testing conditions, thus K_c was computed by considering the maximum load. The results of the NBC–SRIM composites at different crosshead speeds at ambient temperature imply (cf. Fig. 2) that the load–deformation behaviour also strongly depends on the structure and thus on the deformability of the continuous-strand mat reinforcement incorporated.

Increasing temperature generally lowers the K_c of thermoplastic matrices and related composites [7, 8], whereas decreasing temperature increases their K_c values. This trend is also followed in our case (cf Figs. 2 and 3). On the other hand, the effect of the crosshead speed decreases with increasing testing temperature.

Neither the notching direction (T, L), nor the free ligament width (W–a; cf. Fig. 1) of the CT specimens affected the K_c results. The former observation indicates that the GF swirl mat used can be treated as an "isotropic" reinforcement, at least when load transfer is considered in the y–x plane (cf. Fig. 1). The fact that K_c remained within the experimental scatter for the CT specimens of different dimensions and free ligament width indicates that a critical W–a value, if any, should be below 18 mm based on the dimensions of the small CT specimen in Fig. 1. It was concluded from impact studies recently performed on Charpy and Izod specimens that the critical ligament width is about 12 mm [3]. This critical value is related to the possible extension of the damage zone and thus depends both on the local arrangement of the GF mat (surface weight and stacking of the GF mat) and size of the specimens to be tested.

3.2. Failure mode

3.2.1. Failure sequence monitored in situ

Bright-field light microscopic pictures taken during the loading of a CT specimen and the corresponding F–v_{LL} curve are shown in Figs 4 and 5. Based on the serial photographs it is obvious that the notch blunts first (Fig. 4b). With further crack-tip blunting the strands cross the crack-growth plane just ahead of the blunted crack debond, and thus the damage zone extends. Stress whitening of the matrix within this damage zone is caused by ductile tearing and by void formation at the previously debonded sites (dark areas in Fig. 4c and d). The strands intersecting the crack-growth plane, depending on their relative position, either debond further (those under tensile stresses) or split up under fibrillation (those under bending stresses). Strands within the growing damage zone bend and kink due to the local stress field (cf. Fig. 4e and f). These processes take place with concomitant matrix deformation (excessive tearing, voiding and void coalescence) as is obvious in Fig. 4e and f. On exceeding the yield strength of the matrix locally, the bent strands in the damage zone tend to split up, whereas those bridging the flanks of the crack and carrying tensile loads align before final breakage. This occurs in a rather late stage of loading (cf. Fig. 4f and g), which can again be attributed to the mesh-type or network deformability of the GF mat in the very ductile NBC matrix [9].

In order to assign the AE events to those of the observed failure, the F–v_{LL} curve was sectioned as indicated in Fig. 5. This figure displays the positions where the microscopic pictures were taken and also the run of the cumulative AE events. In accordance

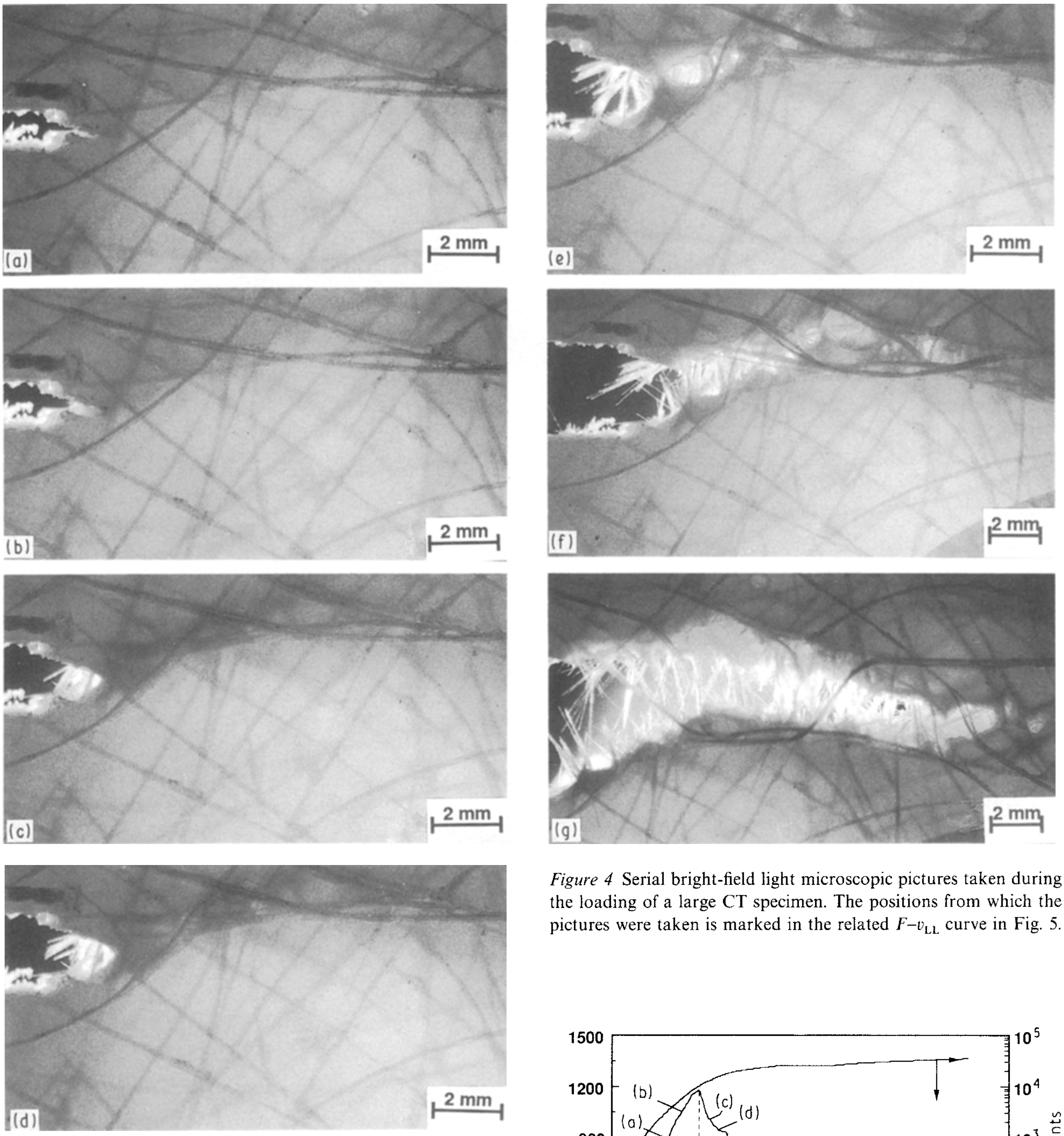

Figure 4 Serial bright-field light microscopic pictures taken during the loading of a large CT specimen. The positions from which the pictures were taken is marked in the related F–v_{LL} curve in Fig. 5.

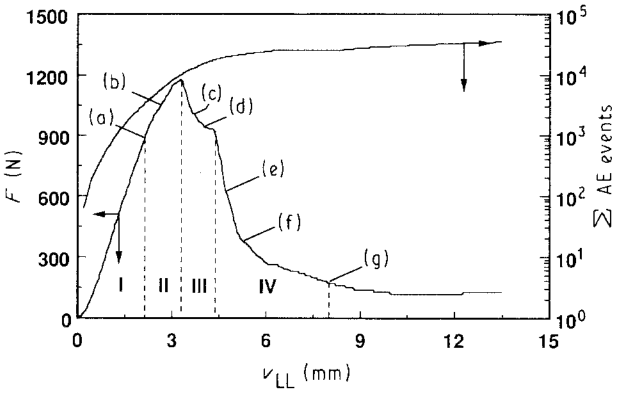

Figure 5 Sectioning of the F–v_{LL} trace and the cumulative run of the AE events registered during static loading of a large CT specimen of NBC-SRIM with 20 wt% GF mat at $T = 20\,°C$ and $v = 1\ \text{mm min}^{-1}$. This figure also illustrates the positions at which the micrographs in Fig. 4 were taken.

with previous findings (e.g. [10–12]) we could discriminate best between the different failure mechanisms observed when the relative distribution of the amplitude and energy of the AE signals were considered. Fig. 6 shows the relative frequency of the AE events as a function of their amplitude and energy for the chosen sections of the loading trace (cf. Fig. 5, I–IV).

Comparison of the evolution of the above AE characteristics (Fig. 6) with those of the failure sequence observed by simultaneous light microscopic monitoring (Fig. 4) during loading of the CT specimen, led to a reliable correlation between them (Table I). A closer look at the results in Table I indicates that the AE values corresponding to the matrix deformation are shifted towards lower values, whereas those of the fibre-related deformation are shifted towards slightly higher values when AE parameters before and after the maximum load are considered. The former observation can be attributed to a change in the deformation mode of the matrix. Debonding along the strand at several sites initiates the formation of voids, followed by their coalescence so that in the damage zone a plane stress state becomes predominant. This stress state enhances the

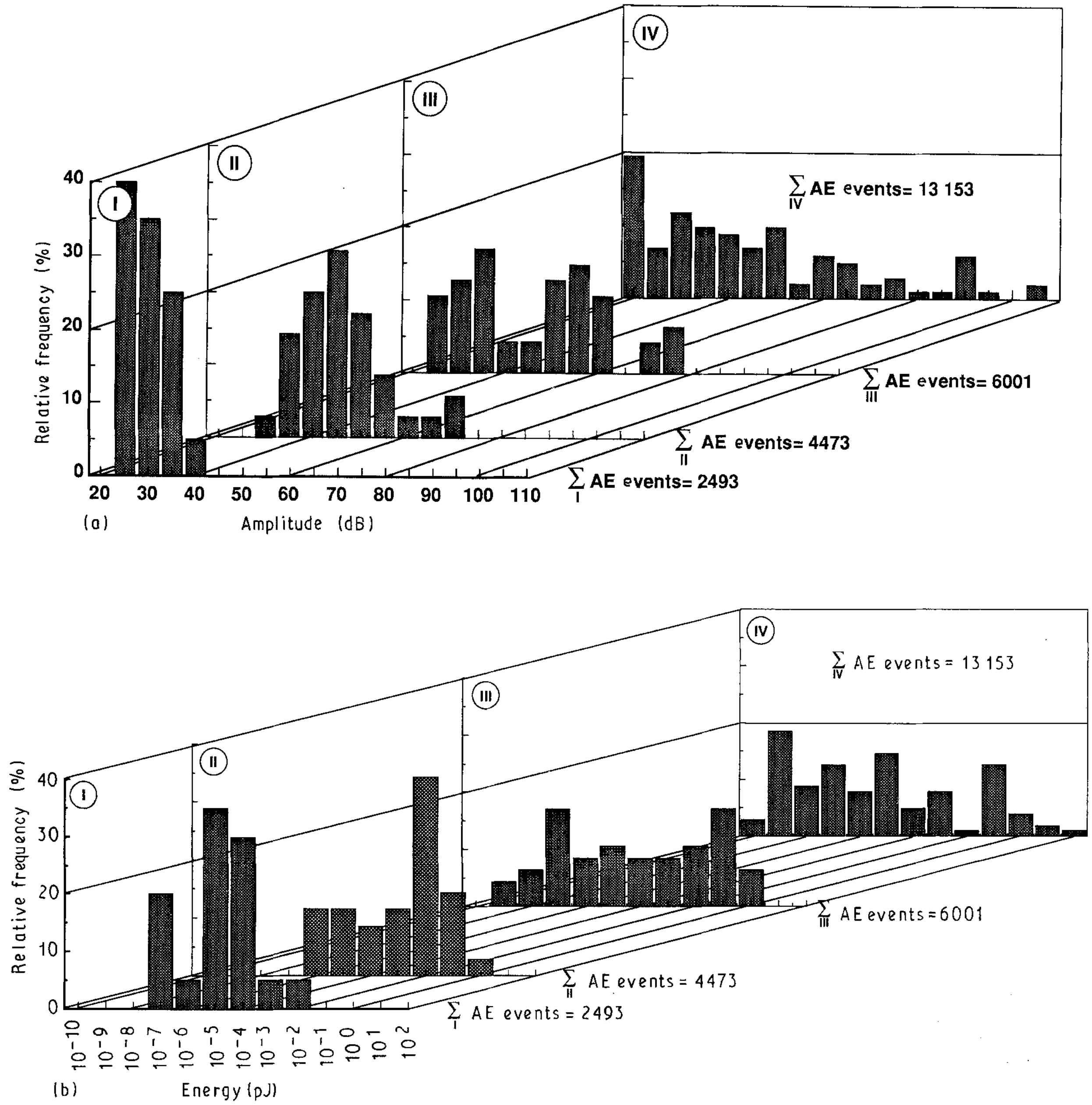

Figure 6 Relative distribution of (a) the amplitude and (b) the energy of the AE events in different sections of the F–v_{LL} curve in Fig. 5. The corresponding light microscopic pictures are given in Fig. 4, and the trace of the cumulative events in Fig. 5.

TABLE I AE assignment of the failure mode observed according to Figs 4–6

Section	Failure mode	Evidence in Fig. 4	AE signals Amplitude (dB)	Energy (pJ)
I	Matrix deformation	(a, b)	< 25	$< 10^{-7}$
	Fibre matrix debonding (short-range)		< 25	10^{-5}–10^{-4}
II	Crack-tip blunting	(b, c)	< 25	10^{-9}–10^{-7}
	Fibre/matrix debonding (short-range and under local stresses)		45	10^{-5}–10^{-3}
	Strand fibrillation and fracture		70	10^{-2}
III	Matrix deformation by voiding	(c, d, e)	< 25	10^{-9}–10^{-7}
	Fibre/matrix debonding (long-range and under local stresses)		55	10^{-5}–10^{-2}
	Strand filamentization and fracture		75	10^{-1}
IV	Matrix deformation by void coalescence and extensive tearing	(e, f, g)	< 20	10^{-10}–10^{-7}
	Short- and long-range fibre/matrix debonding in a "softened" matrix		35 and 50	10^{-5} and 10^{-3}
	Breakage of kinked strands under fibrillation		75	10^{-1}
	Fracture of strands under tensile stresses		> 90	10^{0}–10^{2}

ductility of the NBC by yielding and ductile–viscous flow processes. These matrix deformations on the other hand, lower the AE signals [13]. In order to verify this statement, the failure mode of the neat NBC was studied analogously. Figs 7 and 8 show the F–v_{LL} curve of the matrix together with the cumulated AE events and the relative frequency of the "fractionated" AE parameters, respectively. When the maximum load is reached the crack-tip blunting process is finished (Section I, Fig. 7) and the specimen undergoes extensive tearing, resulting in a pop-in at its surface (Fig. 9). This is a clear indication of a transition from the plane strain to the plane stress state. On the other hand, this transition strongly hinders the onset of secondary cracking. This process is caused by undissolved foreign particles in the (sub) micrometre range and also contributes to the AE signal evolution. Both amplitude and energy of the AE are, therefore, lower when passing the maximum load. In addition, the AE rate is deadened during the tearing process in the postmaximum range (cf. event numbers in Fig. 8).

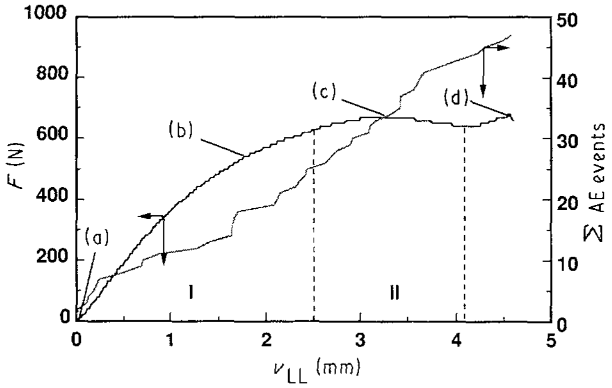

Figure 7 F–v_{LL} curve of the NBC matrix with the related course of the cumulative AE events at room temperature and $v = 1$ mm min^{-1}. This figure also indicates the loading sections selected for AE analysis and the positions which the microphotographs in Fig. 9 were taken.

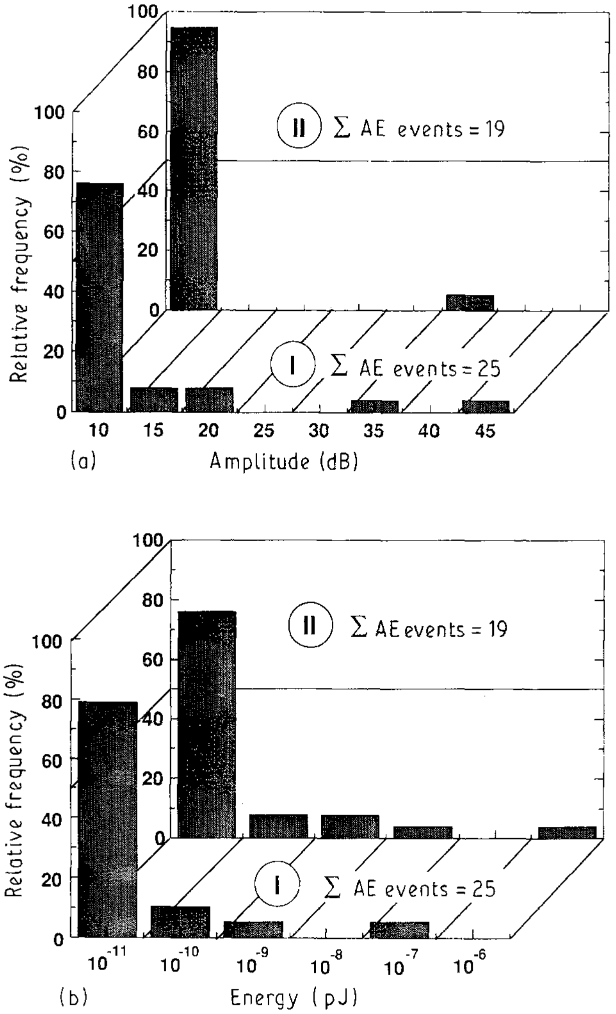

Figure 8 Change in the relative distribution in the AE parameters in the chosen sections of the loading curve of the NBC matrix (cf. Fig. 7): (a) amplitude distribution, (b) energy distribution of the AE signals.

The shift in the fibre-related AE amplitude and energy towards higher values (cf. Table I) can be explained in the following way: the strands bridging

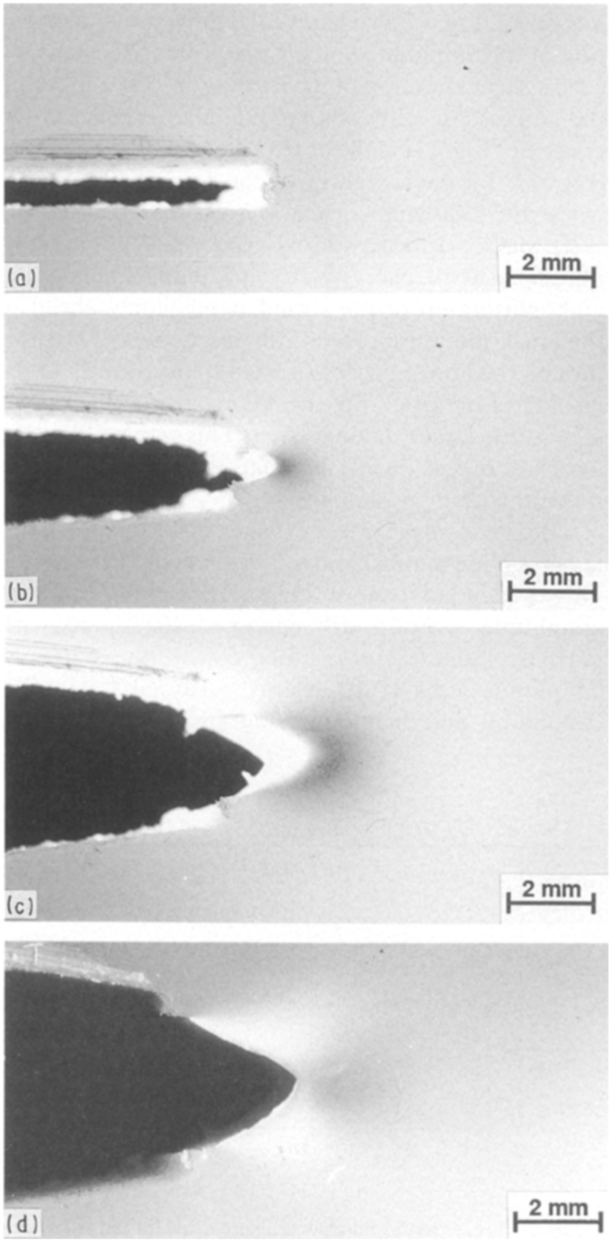

Figure 9 Serial microscopic pictures taken during loading of a large CT specimen of the NBC matrix. The position at which the pictures were taken is indicated in Fig. 7 (a–c). Transmitted light, (d) reflected light showing pop-in phenomenon at the specimen surface.

the flanks of the crack are extended by crack opening and thus carry high local stresses. Further debonding, fibrillation or fracture of these "prestressed" strands originate stronger AE, as was found.

It was demonstrated above (Fig. 4) that the damage zone in the crack tip changes during the test. However, its size and extension can hardly be determined from micrographs because long-range debonding cannot be revealed. An attempt was made to assess the size of the damage zone by AE analysis. For this purpose the localization mode of the AE device with a four-sensor array (cf. Fig. 1) was used. The sound-wave speed was preliminarily determined for the composite plaque with an AE signal generator. Fig. 10 shows the $F - v_{LL}$ curve of the NBC-SRIM with 20 wt% GF mat reinforcement, together with the cumulative AE events, the related bright-field photographs taken during the monotonic loading of the CT specimen are shown in Fig. 11. The evolution of the damage zone deduced from the localized AE events can be followed in Fig. 12. Fig. 12 also shows the differential distribution of the amplitude and energy of the AE events for each selected fraction of the loading trace. Comparing the microscopically observed failure events at the crack tip (Fig. 11) with those of the AE characteristics (Fig. 12) for each section of the force–displacement curve, the following correlations can be deduced.

(I) Matrix deformation by crack-tip blunting (amplitude ≈ 30 dB, energy $\approx 10^{-7}$ pJ) induces debonding and splitting-up of the strand immediately ahead of the crack (amplitude ≈ 60 dB, energy $\approx 10^{-3}$ pJ). Although the above processes seem to occur only in the vicinity of the crack tip, the AE events detected point to a much larger damage area. This implies that the local arrangement of the mat influences the load transfer within the damage zone.

(II) The damage zone extends in both directions. Strands lying parallel and in the plane of further crack growth debond over a longer range and split up (amplitude ≈ 50–75 dB; energy $\approx 10^{-6} - 10^{-2}$ pJ) partially under fracture of their constituting filaments (amplitude ≈ 80–85 dB, energy $\approx 10^{-3}$–10^{0} pJ). This debonding and filamentization process is a rather complicated one including short- and long-range debonding, splitting-up of the strand, fibre/matrix and fibre/fibre friction events) therefore the AE signals cover a broader range. On the left side of the histograms, AE events corresponding to matrix deformations with higher energies can be identified.

(III) In this stage, debonding (amplitude ≈ 40–45 dB, energy $\approx 10^{-6}$ pJ) and splitting-up (amplitude ≈ 60 dB, energy $\approx 10^{-3}$ pJ) processes dominate along the strands lying at a small angle to the crack-growth direction. This results in a horizontal elongation of the damage zone in this stage. Extensive matrix yielding takes place between the debonded sites of the strands running more or less parallel to further crack advance. Owing to the enhanced matrix deformability, AE signals of very low energy appear which are closely matched to those of the neat matrix (cf. Fig. 8)

(IV) In this stage of stable crack propagation, the matrix fails by formation of voids, their collapse and thus by an enhanced tearing (amplitude ≈ 25 dB, energy $= 10^{-9}$–10^{-7} pJ). Among the fibre-related events, strand debonding (amplitude ≈ 60 dB, energy $\approx 10^{-4}$ pJ) and breakage of their constituting filaments suffering under local bending stresses (amplitude ≈ 85 dB, energy $\approx 10^{-2}$ pJ), can be evidenced.

(V) The relative amplitude distribution clearly indicates that in this final stage of fracture, all previously mentioned failure events are involved (matrix deformation with amplitude of ≈ 25 dB; short- and long-range debonding with 50 and 70 dB, respectively; filament fracture of bent strands at 95 dB). Because a further network deformability of the mat is locally hindered and thus strands are extended into the loading direction, they fracture under tensile stresses. This process generates high-amplitude AE signals (amplitude ≈ 95 dB).

The size of the damage zone reaches its maximum at the maximum load. Its further extension along the free ligament relies on crack growth and opening. Thus one can conclude that the load maximum is connected with the development of a critical size of damage zone within which only the relative occurrence of different failure mechanisms changes during further loading. The dimensions of this critical damage zone can be estimated by a circle with a diameter of ~ 22 mm of which ~ 15 mm extends into the unbroken ligament. This value supports our previous finding that K_c was unaffected by the free ligament width of the CT specimens used (being higher than 18 mm; cf. Fig. 1). This value (~ 15 mm) correlates well with that determined from high-speed impact bending tests (12 mm [3]), the scatter is probably an effect of the testing frequency.

The above failure sequence and its assignment to the AE events agree exactly with the previous example (cf. Table I and Figs. 4–6) studied with a single sensor. In addition, the assignment of the failure mechanisms observed with respect to their relative AE amplitude and energy ranking corresponds to the results published in the literature [11, 12, 14, 15].

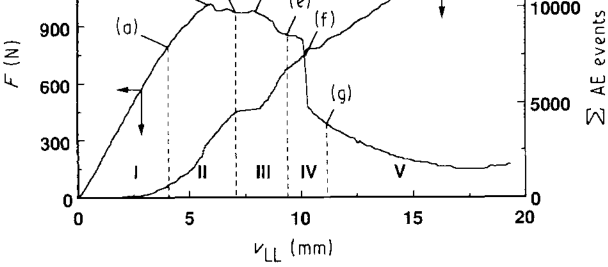

Figure 10 F–v_{LL} curve and the cumulative run of the AE events taken in the localization mode for a modified large CT specimen of an NBC-SRIM with 20 wt% GF mat at room temperature and $v = 1$ mm min^{-1}. This figure displays both the positions at which the microphotographs in Fig. 11 were taken, and the sectioning of the loading curve for AE signal analysis.

3.2.2. Post-mortem failure analysis

The matrix failed microductilely at low temperature

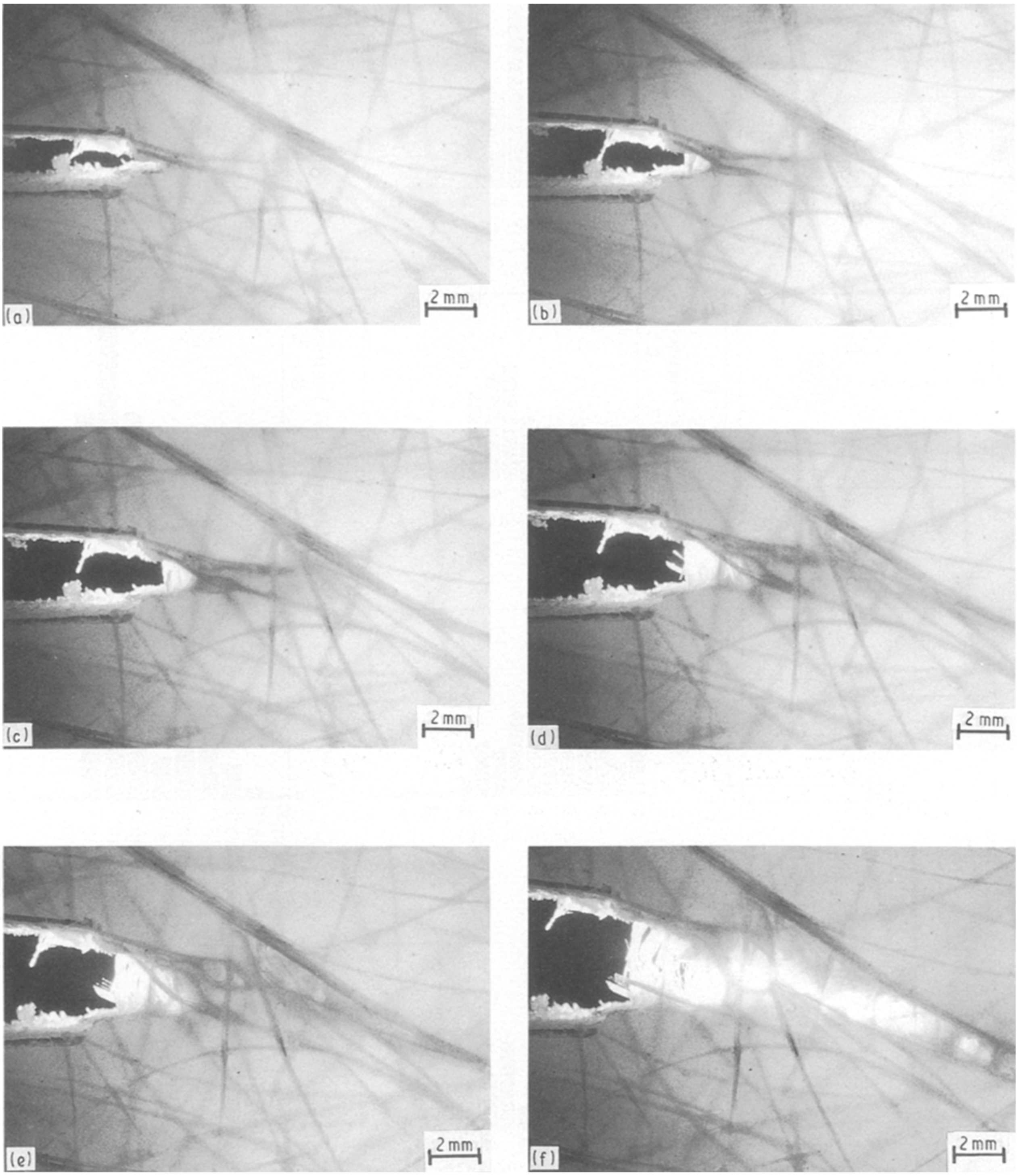

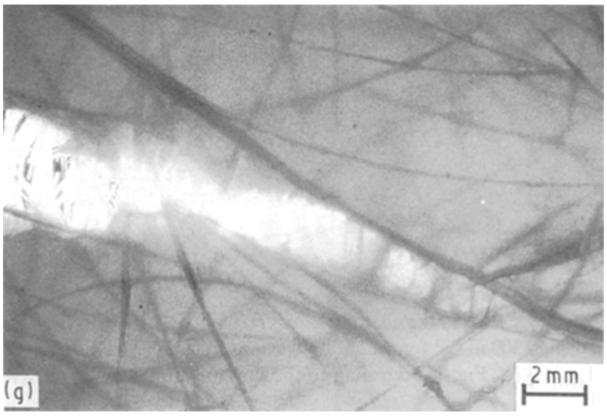

Figure 11 Serial light microscopic pictures taken from the crack-tip region during loading of the CT specimen of NBC-SRIM with 20 wt% GF mat (cf. Fig. 10).

and high crosshead speed (Fig. 13a), whereas viscous tearing was observed at $T = 80\,^{\circ}\mathrm{C}$ (Fig. 13b). In the former case, markings of secondary cracking could also be seen. These parabolic markings contain in their foci areas of undissolved catalyst according to the EDAX traces which exhibit characteristic peaks of magnesium and aluminium, respectively (Fig. 14) [16]. Fig. 13 also shows that secondary cracking is strongly hindered in the plane-stress region indicated by pop-in at the specimen surface. This is an additional reason why AE is decreasing in the postmaximum range (cf. Figs 7 and 8)

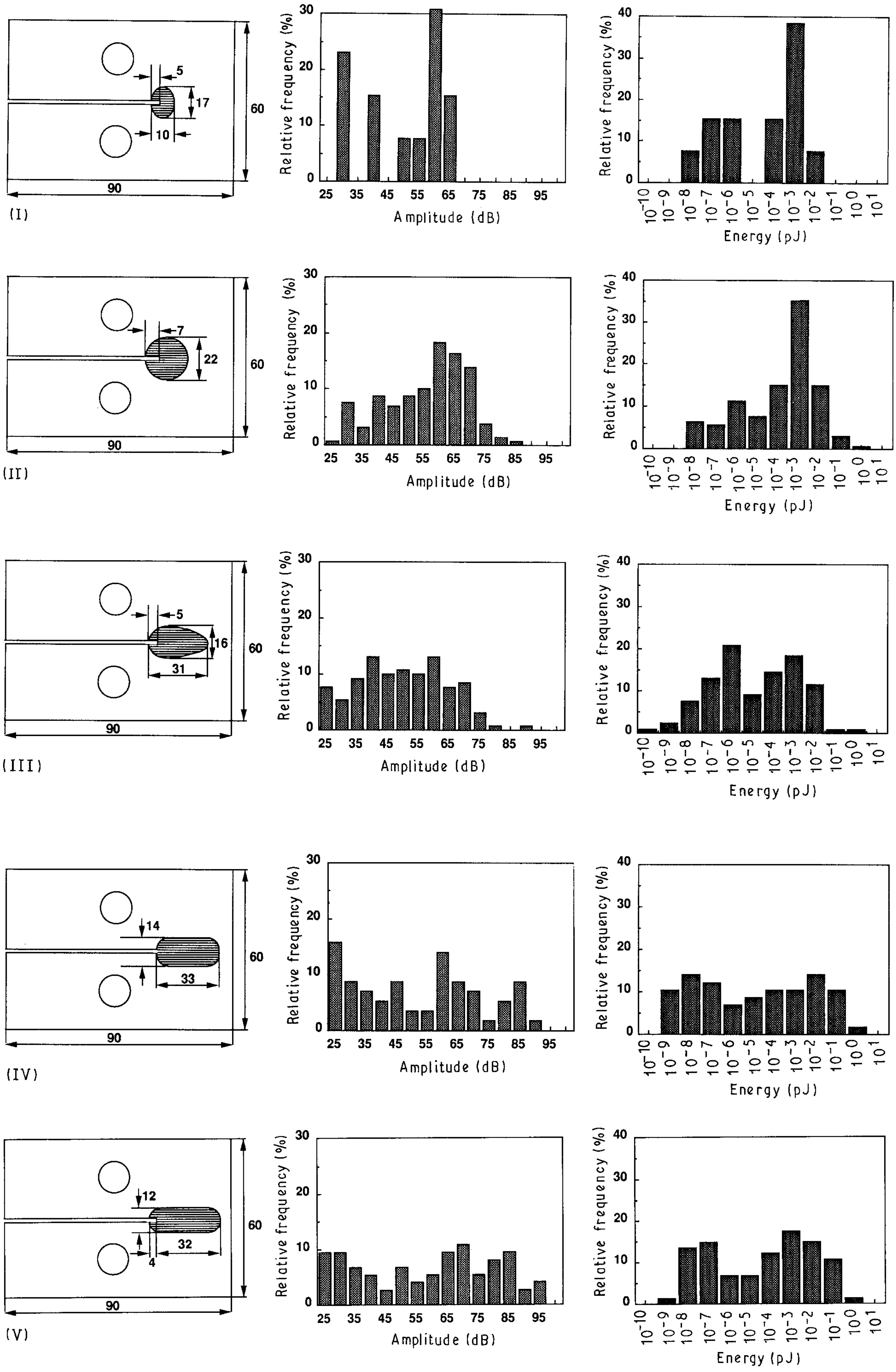

Figure 12 Evolution of the damage zone in different sections of the loading (cf. Fig. 10) and the corresponding relative distribution functions of the amplitude and energy of the AE signals. Localization was performed using 1300 m s^{-1} for the sound-wave propagation, measured by a signal generator. Because practically all events were assessed by sensors 1 and 2 (cf. Fig. 1) according to the first-hit principle, the relative frequency distributions in this figure contain only their cumulative signals.

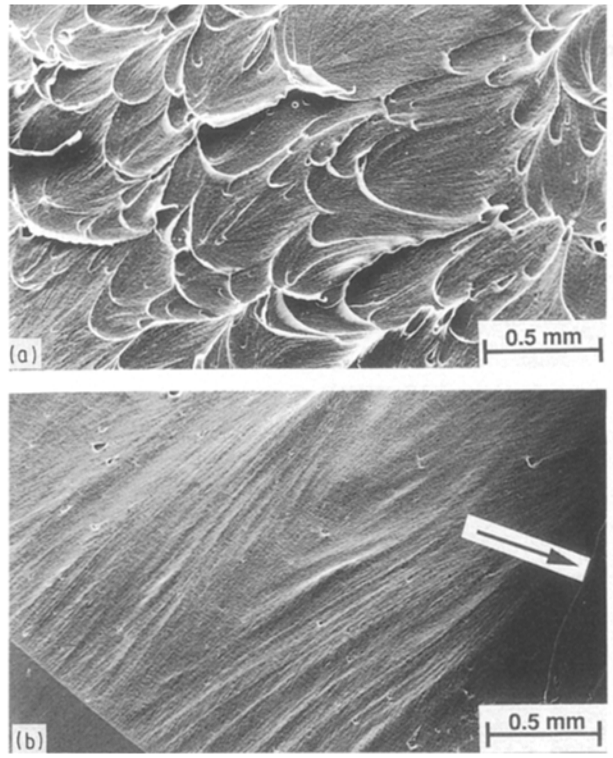

Figure 13 Fracture surface of the unfilled NBC at (a) $v = 1000\ \mathrm{mm\,min^{-1}}$, $T = -40\,^{\circ}\mathrm{C}$; (b) $v = 1\ \mathrm{mm\,min^{-1}}$, $T = 80\,^{\circ}\mathrm{C}$. Arrow indicates the pop-in phenomenon.

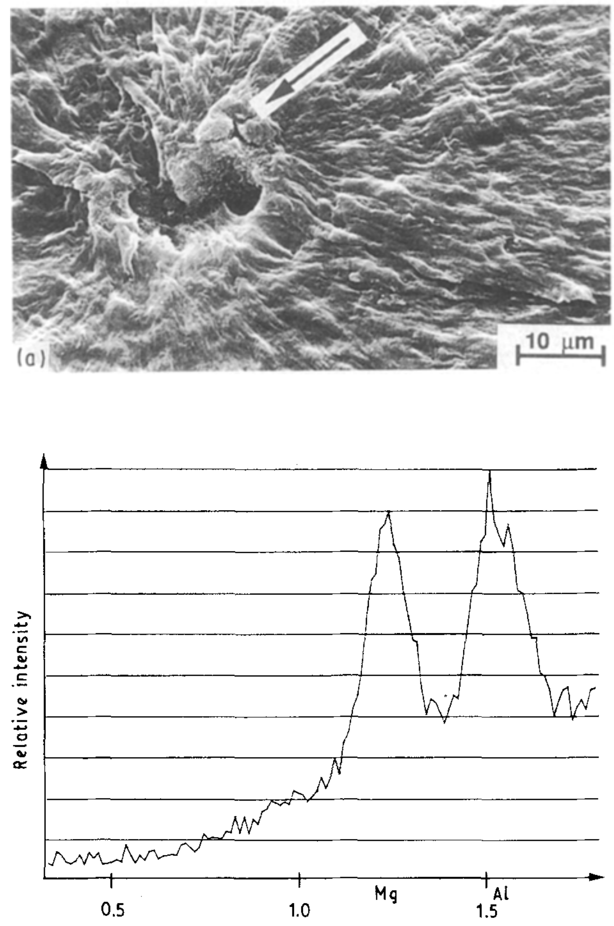

Figure 14 (a) Parabolic marking caused by the secondary cracking phenomenon on the fracture surface of the neat NBC. (b) Identification of the foreign particle in the crater in (a) by EDAX.

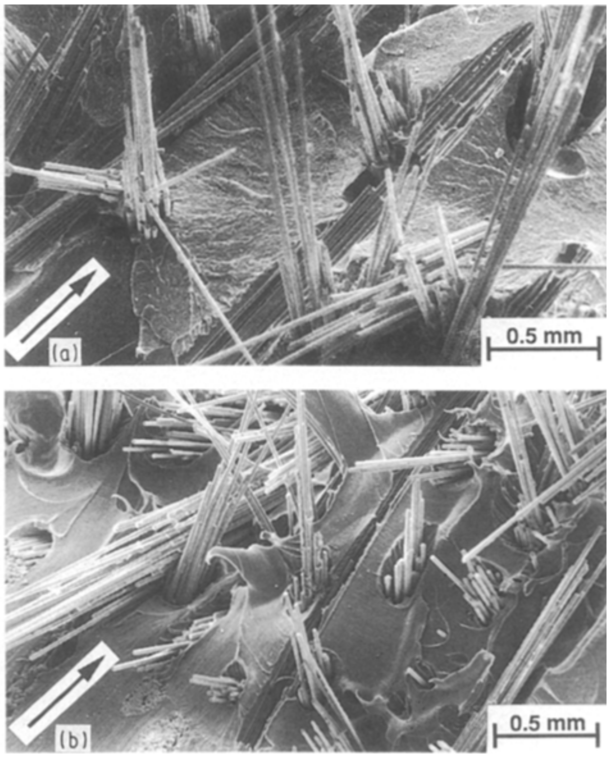

Figure 15 Fracture surfaces of the NBC-SRIM with 20 wt% GF mat reinforcement at $T = -40\,^{\circ}\mathrm{C}$ at different crosshead speeds: (a) $v = 1\ \mathrm{mm\,min^{-1}}$, (b) $v = 1000\ \mathrm{mm\,min^{-1}}$. Arrow indicates the razor blade notch.

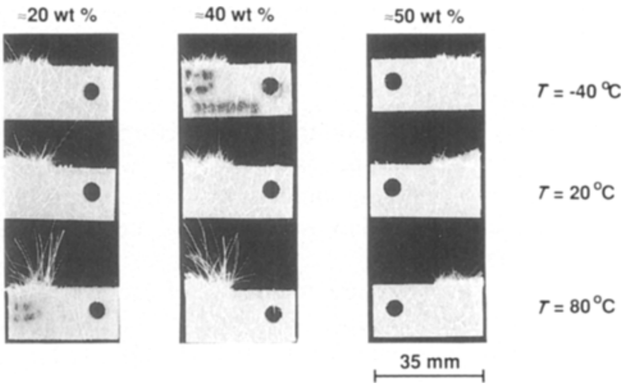

Figure 16 Small CT specimens with various GF mat contents broken at high crosshead speed at different temperatures.

The failure mode of the matrix in the SRIM composites was not affected by presence of the GF mat. In the test at low crosshead speed at $T = -40\,^{\circ}\mathrm{C}$, however, matrix embrittlement was observed for the composite with low GF mat content (Fig. 15a). At higher crosshead speed (Fig. 15b) or GF mat content, the matrix again failed in a ductile manner.

The GF strands fracture upon static loading. The mean pull-out length increases with increasing temperature (Fig. 16) and decreasing crosshead speed, and in addition, its value strongly depends on the GF mat content. This behaviour is connected to an analogous change in the size of the damage zone controlled by the possible local load transfer between the matrix and GF reinforcement. The average length of the pulled-out rovings agrees very well with the critical size of the

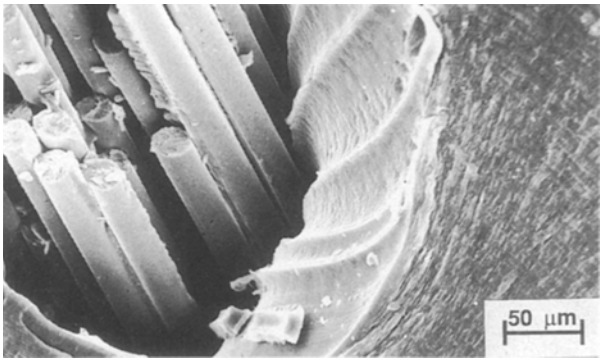

Figure 17 Scanning electron micrograph of a broken strand aligned with the loading direction.

damage zone concluded from the AE analysis (cf. Figs 12 and 16). The scanning electron micrograph in Fig. 17 clearly shows that the fracture of a strand under tensile stress is preceded by a local orientation of the GF mat, which was enabled by a ductile–viscous type deformation of the matrix (cf. tracks in the strand bed in Fig. 17). Fig. 16 also shows that strands inclined at a low angle to the crack plane split-up and fibrillate under the prevaling bending stresses, as shown previously. This produces considerably higher mean pull-out filament length than the breakage of strands by normal plane fracture. In the former case, long-range debonding is also involved.

4. Conclusions

The study carried out on the static fracture behaviour and related failure phenomena of GF swirl mat-reinforced NBC by using simultaneous microscopic and acoustic emission analysis has led to the following conclusions.

1. The static fracture toughness of the GF mat-reinforced NBC is superior to that of the chopped-fibre reinforced composites [7, 16]. The GF swirl mat can be treated as an isotropic reinforcement, provided that the free ligament of the CT specimens lies higher than 15–16 mm. Improvement in the fracture mechanical performance of the GF mat-reinforced NBC composites compared with the chopped-GF reinforced versions, can be attributed to the "continuous" type of the former reinforcement, which induces new energy-absorbing processes by network ("mesh type") deformation. This leads to an extension in the damage zone by stress (re)distribution.

2. A reliable correspondence was found between the failure mechanisms determined microscopically and the amplitude as well as the energy of the AE events. In addition, the AE analysis proved to be an adequate tool for assessing the damage zone and its development. It was shown that the damage zone reaches a critical size at the maximum load. In the crack-propagation stage, its size is practically unaffected (its shape changes only with crack growth) so that only the failure mechanism (relative proportion of different matrix- and fibre-related events to one another) within this zone alters with further loading.

Acknowledgement

The financial support of this study by the EURAM programme of the European Community (MA 1E/0043/C) is gratefully acknowledged.

References

1. J. U. OTAIGBE and W. G. HARLAND, *J. Appl. Polym. Sci.*, **37** (1989) 77.
2. W. S. JOURI and J. B. SHORTALL, *J. Thermoplast. Compos. Mater.* **4** (1991) 206.
3. J. KARGER-KOCSIS, *J. Appl. Polym. Sci.* **45** (1992) 1595.
4. J. KARGER-KOCSIS and K. FRIEDRICH, in "Durability of Polymer Based Composite Systems for Structural Applications", edited by A. H. Cardon and G. Verchery (Elsevier Applied Science, Barking, 1991) pp. 158–68.
5. J. KARGER-KOCSIS, *Polym. Bull.* **24** (1990) 341.
6. *Idem, ibid.* **26** (1991) 123.
7. K. FRIEDRICH and J. KARGER-KOCSIS, in "Solid State Behavior of Linear Polyesters and Polyamides", edited by J. M. Schultz and S. Fakirov (Prentice Hall, Englewood Cliffs, NJ. 1990) Ch.5, pp. 249–322.
8. K. FRIEDRICH, L. A. CARLSSON, J. W. GILLESPIE and J. KARGER-KOCSIS, in "Thermoplastic Composite Materials", edited by L. A. CARLSSON (Elsevier, Amsterdam, 1991) Ch.8, pp. 233–94.
9. J. KARGER-KOCSIS, *J. Polym. Engng* **11** (1992) 153.
10. A. SIEGMANN and R. G. KANDER, *J. Mater. Sci. Lett.* **10** (1991) 619.
11. M. WEVERS, I. VERPOEST, P. DE MEESTER and E. AERNOUDT, in "Acoustic Emission: Current Practice and Future Direction", ASTM STP 1077, edited by W. Sachse, J. Roget and K. Yamaguchi (American Society for Testing and Materials, Philadelphia, PA, 1991) pp. 416–23.
12. J. BOHSE and G. KROH, *J. Mater. Sci.* **27** (1992) 298.
13. C. KAU, A. HILTNER, A. BAER and L. HUBER, *J. Reinf. Plast. Compos.* **8** (1989) 18.
14. H. HANSMANN, *Materialprüfung* **33** (1991) 304.
15. R. K. MILLER and P. MCINTIRE (Eds), "Acoustic Emission Testing, Nondestructive Testing Handbook", Vol. 5 (American Society for Nondestructive Testing, Columbus, OH, 1987).
16. J. KARGER-KOCSIS, in "International Encyclopedia of Composites", Vol. 5, edited by S. M. Lee (VCH, New York, 1991) pp. 337–56.

Received 4 March
and accepted 11 August 1992